Check for updates

Deciphering the doublet luminescence mechanism in neutral organic radicals: spin-exchange coupling, reversed-quartet mechanism, excited-state dynamics†

LingLing Lv, [ID] *[ab] YanYing Zhang[a] and ZiYe Ning[a]

Neutral organic radical molecules have recently attracted considerable attention as promising luminescent and quantum-information materials. However, the presence of a radical often shortens their excited-state lifetime and results in fluorescence quenching due to enhanced intersystem crossing (EISC). Recently, an experimental report introduced an efficient luminescent radical molecule, tris(2,4,6-trichlorophenyl) methyl-carbazole-anthracene (TTM-1Cz-An). In this study, we systematically performed quantum theoretical calculations combined with the path integral approach to quantitatively calculate the excited-state dynamics processes and spectral characteristics. Our theoretical findings suggest that the sing-doublet D_1 state, originating from the anthracene excited singlet state, is quickly converted to the doublet D_1' (trip-doublet) state *via* EISC, facilitated by a significant nonequivalence exchange interaction, with $\Delta J_{ST} = 0.174$ cm^{-1}. The formation of the quartet state (Q_1, trip-quartet) was predominantly dependent on the exchange coupling $3/2J_{TR} = 0.086$ cm^{-1} between the triplet spin electrons of anthracene and the TTM-1Cz radical. Direct spin–orbit coupling ISC to the Q_1 state was minimal due to the nearly identical spatial wavefunctions of the D_1' and Q_1 levels. The effective occurrence of reverse intersystem crossing (RISC) from the Q_1 to D_1 state is a critical step in controlling the luminescence of TTM-1Cz-An. The calculated RISC rate k_{RISC}, including the Herzberg–Teller effect, was 3.64×10^5 s^{-1} at 298 K, significantly exceeding the phosphorescence and nonradiative rates of the Q_1 state, thus enabling the D_1 repopulation. Subsequently, a strong electronic coupling of 37.4 meV was observed between the D_1 and D_2 states, along with a dense manifold of doublet states near the D_1 state energy, resulting in a larger reverse internal conversion rate k_{RIC} of 9.26×10^{10} s^{-1}. Distributed to the D_2 state, the obtained emission rate of $k_f = 2.98$–3.18×10^7 s^{-1} was in quite good agreement with the experimental value of 1.28×10^7 s^{-1}, and its temperature effect was not remarkable. Our study not only provides strong support for the experimental findings but also offers valuable insights for the molecular design of high-efficiency radical emitters.

1. Introduction

Thermally activated delayed fluorescence (TADF) is widely recognized as a third-generation display and lighting technology and has attracted much attention both as an area of theoretical interest and for its potential applications in recent years.[1–4] For TADF materials, the closed-shell molecules are usually chosen as emitters, in which the electrons are paired and filled to the highest occupied molecular orbital (HOMO) in the ground state according to the Aufbau principle.[5] An electron in the ground state is excited from the HOMO and injected into the LUMO (lowest unoccupied molecular orbital), which leads to the formation of both emissive 25% singlet (S_1) and non-emissive 75% triplet (T_1) excitons.[4] To overcome this statistical limitation, with the help of T_1 to S_1 upconversion called reverse intersystem crossing (RISC), TADF can achieve an internal quantum efficiency of nearly 100% in singlet emission.[6,7] However, RISC requires a small energy gap (ΔE_{ST}) between the T_1 and S_1 excited states. This gap is approximately proportional to the electronic exchange interaction (J) between electrons in the HOMO and LUMO, expressed as $\Delta E_{ST} \approx 2J$. Furthermore, the J value is related to the spatial overlap between the HOMO and LUMO.[8] Currently, most TADF emitters often adopt the covalently linked electron donor (D)–acceptor (A) structures for the spatial separation of the HOMO and LUMO to reduce the J interaction. However, this approach presents some unavoidable

[a]School of Chemical Engineering and Technology, Tianshui Normal University, Tianshui, Gansu 741001, China. E-mail: lvling002@tsnu.edu.cn/lvling002@163.com

[b]Key Laboratory of Advanced Optoelectronic Functional Materials of Gansu Province, Tianshui Normal University, Tianshui, Gansu 741001, China

† Electronic supplementary information (ESI) available. See DOI: https://doi.org/10.1039/d4ra03566f

challenges due to the small spatial overlap between the HOMO and LUMO, including a slow fluorescence rate and low fluorescence oscillator strength.[6,7] In addition, D–A type structures are usually flexible and result in significant structural relaxation and a low color purity in their excited states.

Therefore, organic radical emitters are attracting increasing interest as a new type of luminescent materials possessing multiple-spin states and potentially showing spin-luminescence-correlated properties.[5,9–12] Generally speaking, there is now a type of luminescent radical that provides complete spin-allowed emission within a double manifold, such as the tris(2,4,6-trichlorophenyl) methyl-carbazole (TTM-Cz) and 9-(naphthalene-2-yl)-9H-carbazole (TTM-3NCz) emitters.[13–16] These radical emitters provide a simple way to prevent 75% energy loss from the first-generation organic light-emitting diodes (OLEDs) based on traditional organic emitters. Unfortunately, currently most stable radicals are non-emissive, because their high-spin structures have high (approximately 1 eV) energy gaps between the photogenerated donor singlet state and the triplet manifold. Essentially, this prevents the RISC process from a dark state to a luminescent state.[17,18]

Additionally, in quantum-information science and technology, recent studies have also shown that strongly coupled photogenerated triplet-radical systems can be used as multi-level spin qubits, *i.e.*, qubits, such as the perylene-diimide-2,2,6,6-tetramethylpi-perdiny-1-oxyl (PDI-TEMPO) stable radical.[17–20] It is well known that electron spins are good qubits because the two spin states can exist in a superposition, and coupling two or more spins *via* spin–exchange coupling and/or zero-field interactions leads to versatile spin physics.[21] However, as with all such systems, the primary challenge is that the high-spin structure also has a large energy difference between the quartet ('trip-quartet', $S = 3/2$) and doublet ('trip-doublet', $S = 1/2$) states, resulting in the RISC to a luminescent state becoming impossible, which prevents optical readout *via* emission.[17,18]

In order to overcome the limitations of the optical readout or luminescence above, Evans and co-workers put forward a novel design strategy,[17] which involved introducing an energy resonance between the emissive doublet and donor triplet levels. To put it another way, the vital idea of this design strategy was to bring the donor triplet T_1 level into energy resonance with a luminescent radical doublet D_1 level based on a class of luminescent radicals that provide absolutely spin-allowed emission within the doublet manifold. Employing this strategy, they designed and synthesized an excited-state complex with a near-unity generation yield, specifically tris(2,4,6-trichlorophenyl)methyl-carbazole-anthracene (TTM-1Cz-An), as depicted in Fig. 1. Here, reducing the large energy gap between the emission state and the high-spin state enabled interconversion *via* RISC to emissive states, thereby making it possible to achieve luminescence from high-spin states with $S > 1$ in organic radical molecules.

Compared to the experimental study of Evans and co-workers,[17] up to now, there seems to have been relatively scarce theoretical exploration to provide a comprehensive and in-depth understanding of this original design strategy, especially, the influence of high-spin state RISC on the overall
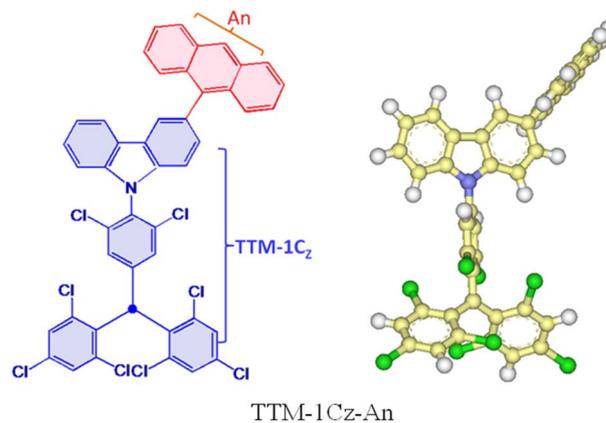

Fig. 1 Molecules featured in the covalent coupling of the tris(2,4,6-trichlorophenyl)methyl-carbazole radical (TTM-1Cz) and anthracene (An) studied in this work.

luminescence mechanism. To design a new generation of efficient radical emitters for OLEDs, we require a detailed understanding of the factors that govern the fluorescence characteristics of organic radicals at the molecular level. Consequently, in this investigation we systematically and quantitatively studied the excited-state dynamics of the TTM-1Cz-An system by applying time-dependent density functional theory combined with the path integral approach, to provide a quantitative understanding of the radical luminescence mechanism. Our motivation was to provide theoretical support for designing novel radical luminescent materials.

2. Computational details

2.1 Geometric structures and electronic properties

All calculations were performed using the ORCA 5.0.4 program.[22] Geometry optimizations were performed with the range-separated hybrid ωB97X-D3 and CAM-B3LYP functionals and the Ahlrichs polarized def2-SVP basis sets, combined with the corresponding def2/J auxiliary basis sets for the RIJ approximation to the Coulomb integrals, while the exchange terms were efficiently accelerated using the "chain-of-spheres" (COSX) algorithm.[23–28] The integration grids employed the default set (DEFGRID2) in the ORCA nomenclature, with tight energy convergence settings applied throughout the calculations.[22] The surroundings were described with the conductor-like polarizable continuum model (C-PCM) with toluene solvent.[29] Numerical frequency analysis was performed for all the optimized structures, and there were no imaginary vibration modes to ensure that the obtained structure was a local minimum on the potential energy surface (PES). In addition, the corresponding Hessian data were subsequently used for the excited-state dynamics calculations. In order to further improve the calculation of the doublet–doublet excitation energies, single point energies were recalculated using the range separation, and spin-component/opposite scaling (SCS/SOS), time-dependent double-hybrid density functionals, including SCS-ωB2GP-PLYP and SCS/SOS-ωB2PLYP, in conjunction with the larger def2-TZVP basis set, where applicable, and the corresponding auxiliary def2-TZVP/C

and def2/J basis sets.[30–32] Under the same conditions, the domain-based local pair natural orbital approach, and coupled cluster calculations (*e.g.*, DLPNO-CCSD(T)) were also be applied to the single point energy calculations.[33,34]

2.2 Exchange coupling and zero-field splitting

The excited-state exchange–coupling interaction (J_{TR}, where the subscript T denotes the anthracene triplet state, and R is the TTM-1Cz radical) was calculated using QD-NEVPT2/def2-TZVP on optimized CASSCF wavefunctions, where the selection of the active space is important to first understand the nature of the low-lying excited states by carefully assessing their orbital contributions. The starting orbitals of the CASSCF calculation,[35] were obtained using TD-DFT at the ωB97X-D3/def2-TZVP level of theory with the RIJCOSX approximation for the Coulomb- and exchange integrals.[23,25–28] TD-DFT provides rapid and comprehensive insights into the orbitals that play a crucial role in the excited-state mechanism, subsequently allowing defining the active space in the CASSCF calculation. The excited states of interest primarily originate from electronic transitions occurring within both the HOMO and LUMO orbitals of the anthracene, as well as the SOMO (single occupied molecular orbital) of the TTM-1Cz radical. Consistent with expectations, the active space in the CASSCF calculation, denoted as (3, 3), encompassed three electrons distributed in three orbitals, specifically, anthracene's HOMO and LUMO, along with the radical's SOMO. The minimal active space is instrumental in providing a qualitatively accurate portrayal of these states, ensuring that the fundamental characteristics of the excited states are captured effectively. The optimized active orbitals were localized by the Foster–Boys method for an easier interpretation of the excited states.[36]

The excited-state exchange coupling J_{TR} between the anthracene triplet state and the TTM-1Cz radical doublet state can be calculated using the following formula:[37]

$$J_{TR} = 2/3(E_{D_1} - E_{Q_1}) \tag{1}$$

or approximated as:

$$J_{TR} = \frac{J_{12} + J_{13}}{2} \tag{2}$$

where the subscripts 1, 2, and 3 for J refer to the electrons in the radical SOMO of the TTM-1Cz, and the HOMO and LUMO of the anthracene, respectively. Also, the individual exchange interactions (J_{12}, J_{13}, and J_{23}) were extracted by a numerical effective Heisenberg–Dirac–van Vleck Hamiltonian,[38] see eqn (3), and the corresponding extraction details were shown recently in ref. 37.

$$\hat{H}_{HDVV} = -J_{12}\hat{S}_1\hat{S}_2 - J_{13}\hat{S}_1\hat{S}_3 - J_{23}\hat{S}_2\hat{S}_3 \tag{3}$$

To characterize the mixed information of the excited quartet (Q_1) and doublet (D_n) states by electron dipolar induction, the zero-field splitting (ZFS) interaction, which can be characterized by the aid of the two ZFS parameters D and E,[39,40] was calculated using the ORCA 5.0.4 program at the ωB97X-D3 and CAM-B3LYP/def2-TZVP levels. The spin–orbit coupling (SOC) was

calculated using the quasi-degenerate perturbation theory at the CASSCF (7,5)/def2-TZVP level. The selection of the active orbitals was guided by the same principles previously discussed for the CASSCF(3,3) method. Specifically, the TD-ωB97X-D3 calculation identified several orbitals that are pivotal to the mechanism of the excited state. These orbitals were then incorporated into the active space, which consisted of 7 electrons in 5 orbitals: the HOMO and LUMO of anthracene, along with the SOMO of the radical, and the two orbitals immediately below the HOMO, known as HOMO-1 and HOMO-2. The corresponding active orbitals are presented in Table S1 of the ESI.†[41] In this approach, the SOC operator was handled with the efficient mean-field (SOMF) approximation to the Breit–Pauli operator (SOCType 3 in ORCA 5.0.4),[41,42] called RI-SOMF, which makes use of the RI scheme to accelerate Coulomb integrals. Additionally, the gradient of the SOC matrix elements ($\partial\langle SOC\rangle/\partial Q_k$, where Q_k is a mass-weighted normal coordinate) with respect to the normal modes was estimated using a finite-difference method.[43] Here, the optimized structure at $Q_k = 0$ was used to construct the molecular configuration, which was displaced along the vital normal mode by increments of 0.1 dimensionless normal coordinates.

2.3 Nonradiative decay rate

The nonradiative decay rate constants (k_{IC}) were estimated by means of the Marcus–Levich–Jortner approach, with its one-effective mode equation expressed as:[10,44]

$$
\begin{aligned}
k_{IC} = {} & \frac{2\pi}{\hbar}\left|V_{D_{n,m}}\right|^2 \frac{1}{\sqrt{4\pi\lambda_M k_B T}} \\
& \times \sum_{n=0}^{\infty} e^{-S_{eff}}\frac{S_{eff}^{\,n}}{n!}\exp\left[-\frac{\left(\Delta E_{D_n-D_m} + \lambda_M + n\hbar\omega_{eff}\right)^2}{4\lambda_M k_B T}\right]
\end{aligned}
\tag{4}
$$

where $\hbar$, k_B, and T, are the reduced Planck constant, the Boltzmann constant, and temperature, respectively; $V_{D_{n,m}}$ is the electronic coupling interaction between the excited states (D_n and D_m), which was computed by the two-state generalized Mulliken–Hush approximation;[45] ω_{eff} and S_{eff} are the effective vibrational frequency and corresponding Huang–Rhys factor, and they describe the quantum effect of the high-frequency normal modes by a single effective mode; and n is the vibrational quantum number of this effective mode.[46,47] ω_{eff} and S_{eff} were calculated using the following equations:

$$S_{eff} = \sum_i S_i \tag{5}$$

$$\omega_{eff} = \frac{\sum_i S_i\hbar\omega_i}{S_{eff}} \tag{6}$$

where λ_M is the classical reorganization energy that comes from the low-frequency vibrations ($\hbar\omega_M < 1000\ \text{cm}^{-1}$), and $\Delta E_{D_n-D_m}$ denotes the adiabatic energy between the doublet excited D_n and D_m states.

For the ISC and RISC rates, k_{ISC} and k_{RISC} were computed using the ORCA_ESD module with default settings within the ORCA 5.0.4 package.[22,48,49] The harmonic approximation to the PESs was based on the adiabatic Hessian model. It was assumed

that the geometries and Hessians of the quartet Q_1 and doublet D_1 spin sublevels were the same.

2.4 Radiative rate and fluorescence spectrum

Within the framework of the Born–Oppenheimer approximation, the spin-allowed radiative rates (k_f) between an initial state i and a final state f were determined using Fermi's golden rule, which encompasses integrates across the entire radiative spectrum. The corresponding equation, expressed in atomic units, is as follows:[48,49]

$$k_f(\omega) = \frac{2\omega^3}{3\pi c^3 Z} \sum_{if} e^{-\frac{\varepsilon_i}{k_B T}} \langle \Theta_i | \mu | \Theta_f \rangle \langle \Theta_f | \mu | \Theta_i \rangle \int e^{(iE_i - E_f - \omega)t} dt \quad (7)$$

where ω represents the photon energy; μ is the electronic transition dipole; $|\Theta\rangle$ denotes the vibrational wavefunction of either the initial or final state; $e^{-\frac{\varepsilon_i}{k_B T}}/Z$ describes the initial state Boltzmann population at temperature T; ε_i is the total vibrational energy of initial state; and Z represents the vibrational partition function. After further manipulations, eqn (7) was ultimately transformed into a Discrete Fourier Transform (DFT) of a correlation function $\chi(t)$ with a time step Δt.[49] The transformed formula is given by:

$$k(\omega) = \frac{2\omega^3}{3\pi c^3 Z} \Re e \int_0^\infty \chi(t) e^{-i\omega t} dt$$

$$= \frac{2\omega^3}{3\pi c^3 Z} \Delta t \Re e \mathrm{DFT}[\chi(t)] \quad (8)$$

The $\chi(t)$ function was subsequently computed analytically at each time point t using "path integral methods".

In our calculations, vibronic coupling, the so-called Herzberg–Teller (HT) effects, was considered by expanding the matrix elements of the $\mu(Q_k)$ with respect to the normal coordinate Q_k,[50] as shown below:

$$\mu(Q_k) = \mu_0 + \sum_k \left. \frac{\partial \mu}{\partial Q_k} \right|_{Q=0} Q_k + \dots \quad (9)$$

In this expression, the μ_0 term corresponds to the traditional Frank–Condon (FC) approximation, which keeps only the coordinate-independent term, whereas the second term represents the HT contribution.

3. Results and discussion

3.1 Resolved absorption spectra

To comprehensively understand the nature of the excited states of the TTM-1Cz-An compound, the vibrationally resolved
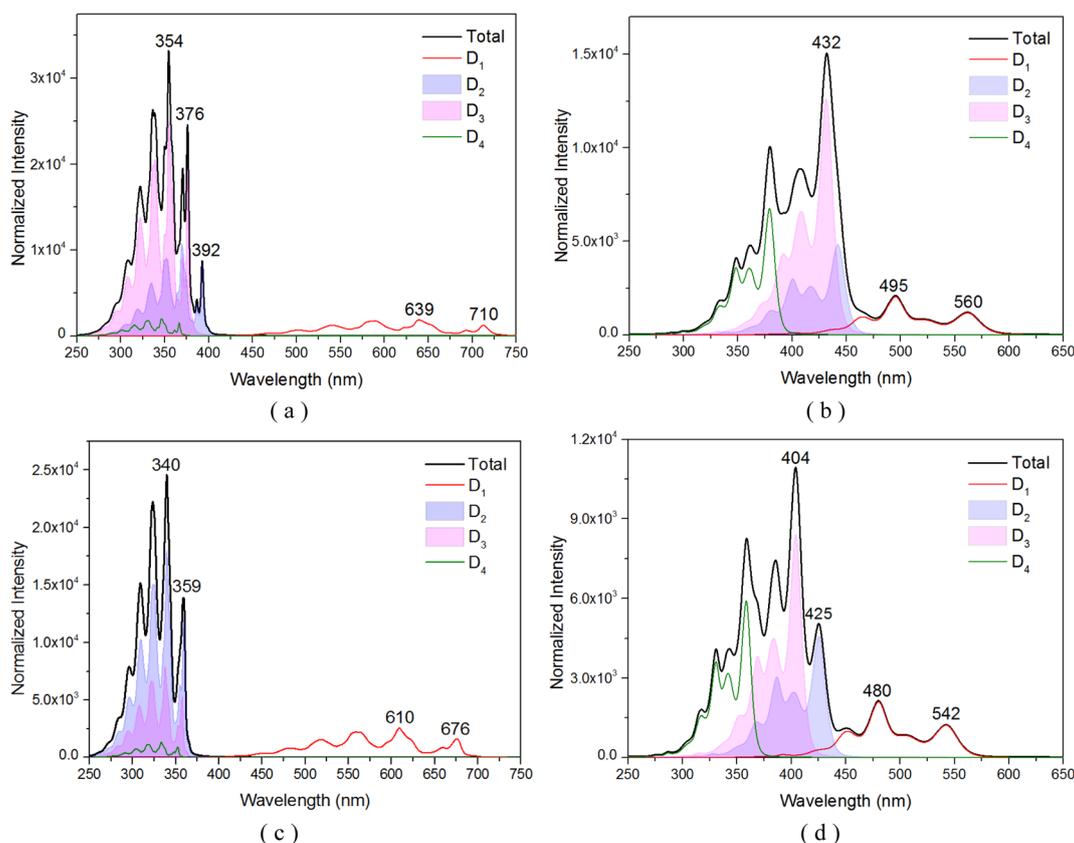

Fig. 2 Vibrationally resolved absorption spectra of several key doublet excited states for TTM-1Cz-An: (a) obtained at the CAM-B3LYP/def2-TZVP level in the toluene solvent, and (b) in the gas phase; (c) and (d) were obtained using the ωB97X-D3 method under liquid and gas environments, respectively.

© 2024 The Author(s). Published by the Royal Society of Chemistry

absorption spectra for the transition from the doublet ground D_0 to the different excited states with D_1, D_2, D_3, and D_4 were simulated in the gas and liquid phases, as shown in Fig. 2, which is helpful to elucidate the underlying nature of the experimental phenomenon. Specifically, in the case of the toluene solution, for the absorption profiles for the $D_0 \rightarrow D_1$ transition (Fig. 2a), two prominent features were observed: a mountainous extension from 500 to 725 nm, and the main peak centered at 639 nm, both of which were in quite good agreement with experimental data of about 685 nm.[17] At the level of the ωB97X-D3 theory, almost identical spectral data were obtained, as shown in Fig. 2c. Interestingly, the sharp peak at 354 nm (or 340 nm), corresponding to the high energy vibrational range, was primarily due to the excitation of two nearly degenerate electronic states, D_2 and D_3, which was in qualitative agreement with experimental value of 374 nm.[17] We also noticed that these vibrational spectral bands significantly overlapped, which allows for the possibility for these states to undergo fast internal conversion (IC) through interactions such as SOC, configuration interaction, or possibly vibronic coupling. Moving to the gas phase, as could be noted by comparing Fig. 2b and d, the spectral band was relatively discrete, and the $D_0 \rightarrow D_1$ transition significantly deviated from the experimental data of 685 nm.[17] Also, the D_2 and D_3

excitations showed an overall redshift of the energies relative to the experimental data.

3.2 Characterization of the excited states

Fig. 3 indicates electronic spin configurations of TTM-1Cz-An with the occupancies of the high-lying occupied and low-lying unoccupied orbitals, which were composed of three orbitals (HOMO−4, HOMO−1, and SOMO) in the located TTM-1Cz radical, of which two π-type orbitals (HOMO and LUMO) of the An unit, the corresponding natural transition orbitals, are displayed in Tables S1–S3 of the ESI.† The doublet ground state D_0 has an unpaired electron primarily located on the SOMO, following the conventional Aufbau principle.[5,10] In other words, the energy of the SOMO is generally located above the doubly occupied HOMO and below the LUMO. A critical electronic excitation can be described as a HOMO → LUMO transition (Fig. 3), resulting in the D_1 excited state (i.e., sing-doublet state), which corresponds to the first excited singlet state S_1 of anthracene upon light absorption. It exhibited a very small transition dipole moment of 0.0003 a.u. due to the parity-forbidden nature based on group theory considerations. In the presence of the radical, the triplet sublevel state $T_{1,0}$ (where 0 is the spin magnetic quantum number) of anthracene may then be generated by radical-enhanced intersystem crossing
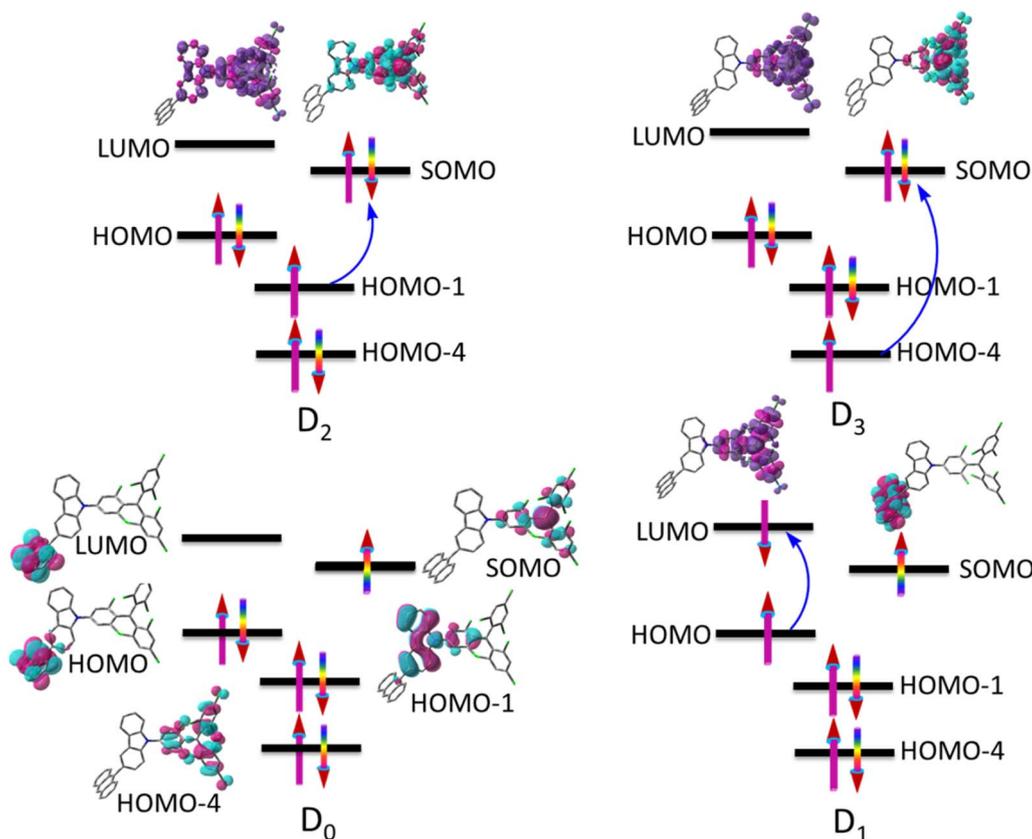

Fig. 3 Electronic spin configurations of the TTM-1Cz-An compound consisting of the doublet TTM-1Cz radical and the singlet An (anthracene). For the ground state D_0, the vital natural active orbitals are inserted into the figure; the formation of excited states (D_1, D_2, and D_3) in the electronic transitions is marked with blue arrows, and the spin density and transition density difference are separately displayed in the upper part of the configuration.

(EISC),[37,51] and then the anthracene triplet state and radical doublet state will interact, with the details discussed below. As for the D_2 and D_3 excitations, they can be characterized as either a HOMO-1 → SOMO or HOMO-4 → SOMO transition, respectively. These excitations were localized in the TTM-1Cz radical fragment and exhibited strong transition dipole moments of 0.915 and 0.547 a.u. at the ωB97X-D3 level, respectively. To further characterize the rationality of the excitation configuration, the excited-state spin density and transition density difference are separately displayed in the upper part of the configuration, see Fig. 3 and Table S4 in the ESI,† which more reliably support the nature of the electron excitation.

3.3 EISC and quartet state (Q_1) formation

It is known that the EISC is a spin-allowed process due to the overall spin multiplicity conservation within the photoexcited TTM-1Cz-An radical system. The singlet excited state of anthracene, which involved a transition from the HOMO to LUMO (HOMO → LUMO), known as a sing-doublet state D_1, was converted to a trip-doublet state $D_1^{'}$ This conversion occurs by nonequivalent spin–exchange coupling of the singlet excited electrons of anthracene and the third radical electron mediated. This mechanism is referred to as the ΔJ_{ST} mechanism,[52] where ΔJ_{ST} is defined as $(J_{13} - J_{12})/2$, and was calculated to be

0.174 cm^{-1} at the CASSCF/QD-NEVPT2 level, as detailed in Table 1. This process is schematically depicted in Fig. 4, with the corresponding visualization of the localized spin centers illustrated in Fig. 5.

As can be seen from Fig. 4, the electrons in the LUMO of anthracene and the SOMO of the radical simultaneously flip their orientation through exchange coupling. This change conserves the overall doublet spin multiplicity while generating a local triplet state on the anthracene fragment, resulting in the $D_1^{'}$ state. The formation of the quartet state (Q_1, trip-quartet) predominantly relies on the exchange–coupling interaction J_{TR} between the triplet spin electrons of anthracene and the TTM-1Cz radical.[37,50] If the J_{TR} interaction surpasses all other magnetic interactions within the TTM-1Cz-An radical system, the Q_1 state can be formed through spin mixing. The data in Table 1 indicate that the exchange interaction, with a value of $J_{TR} = 0.057$ cm^{-1} at the CASSCF/QD-NEVPT2 level (see out file of the J_{TR} calculation in the ESI†), was sufficiently large to enable the formation of the Q_1 state *via* spin exchange. It could also be noted that the J_{TR} was positive, suggesting that the TTM-1Cz-An radical exhibits ferromagnetically coupling,[50,51] which implies that the Q_1 state was energetically favored over the $D_1^{'}$ state.
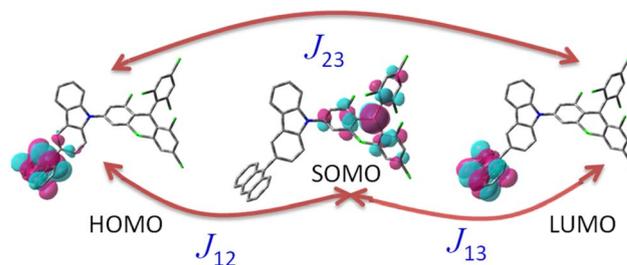
Table 1 Calculated exchange coupling constants (J cm^{-1}) of the investigated TTM-1Cz-An molecular system at the CASSCF (3, 3)/def2-TZVP level. The subscripts 1, 2, and 3 refer to the electrons in the radical SOMO of the TTM-1Cz, and the HOMO and LUMO of anthracene, respectively[a]

Method	J_{12}	J_{13}	J_{23}	J_{TR}	$J_{TR}^{'}$
CASSCF/QD-NEVPT2	−0.116	0.232	12 300.1	0.058	0.057
CASSCF	−0.736	0.544	45 215.4	−0.096	−0.095
ROCIS					−49.761

[a] $J_{TR} = (J_{12} + J_{13})/2$; $-3/2J_{TR} = E(Q_1) - E(D_1)$.

Fig. 5 Exchange interactions (J cm^{-1}) illustration of the three-electron-three-center problem, including assignment of the orbitals for the investigated TTM-1Cz-An system. The subscripts 1, 2, and 3 refer to the electrons in the radical SOMO of TTM-1Cz, and the HOMO and LUMO of anthracene, respectively.
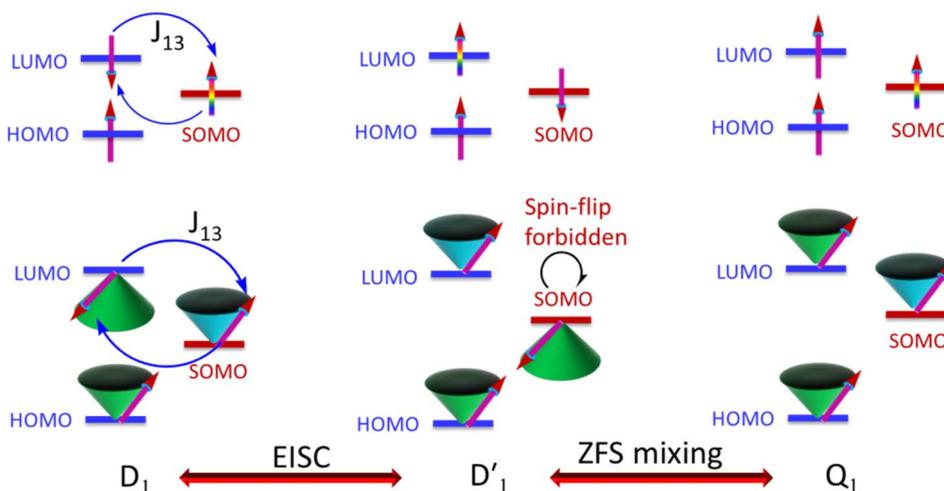

Fig. 4 Simplified vector picture of the EISC process generating a local triplet state on anthracene by dipolar-mediated interactions.

Regarding the individual contributions to J_{TR}, it could be seen that both absolute magnitudes (J_{12} and J_{13}) were bigger for the TTM-1Cz-An radical, and this can be explained by visualizing the spin center in a relatively direct manner, see Fig. 5. The interpretation of the reverse sign of the J_{12} and J_{13} interactions is more sophisticated, and the sign was likely decided by the symmetry of the individual spin centers.

3.4 ISC and RISC processes

3.4.1 $D_1' \leftrightarrow Q_1$ ISC. Even though D_1' and Q_1 were well separated by an energy gap of $3/2 J_{TR} = 0.086$ cm^{-1}, as shown in Fig. 6, the ZFS interaction, denoted as H_{ZFS}, of the two unpaired electrons localized on anthracene leads to a mixing of the D_1' and Q_1 states:[39,40]

$$H_{ZFS} = D(S_z^2 - S^2/3) + E(S_x^2 - S_y^2) \quad (10)$$

where D and E are the ZFS tensors. The rate of ISC from the spin sublevels of D_1' to those of Q_1 is dependent on the prohibition factor, which is associated with the change in spin, denoted as f_s (m_2, m_4), with $m_2 = \pm 1/2$, and $m_4 = \pm 1/2, \pm 3/2$, respectively:[53]

$$f_s(m_2, m_4) = \frac{\left| \langle Q_1(m_4) | H_{ZFS} | D_1'(m_2) \rangle \right|^2}{\left(E_{Q_1(m_4)} - E_{D_1'(m_2)} \right)^2} \quad (11)$$

where the $f_s(m_2, m_4)$ term characterizes the spin-dependent transition strength due to the H_{ZFS} perturbation that mixes D_1' and Q_1. This H_{ZFS} perturbation is often quantified by the ZFS tensors of D and E. The calculated D and E values at the ωB97X-D3/CAM-B3LYP levels are detailed in Table S5 of the ESI,† and the D tensor orientation and spin density of the quartet Q_1 state are depicted in Fig. 7.

The ZFS tensors for TTM-1Cz-An were calculated to be $D = -0.026$ cm^{-1} and $E = -0.005$ cm^{-1} (Table S5†). The E value was extremely small, implying a negligible spin density distribution difference between the D_{xx} and D_{yy} directions, as can be seen in Fig. 7. Meanwhile, the substantial D value stemmed from the SOC contribution of -0.0296 cm^{-1} at the ωB97X-D3 level, which
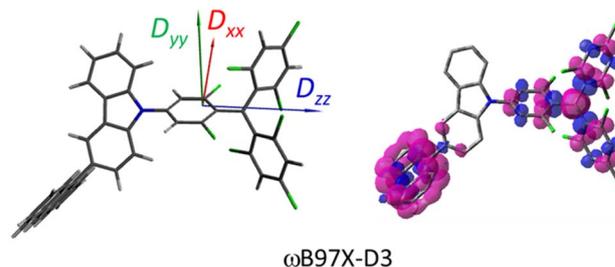

Fig. 7 Drawing of the ZFS tensor (D) orientations and spin density (right) of TTM-1Cz-An for the quartet Q_1 state.

accounted for approximately 88% of the total D value, as shown in Table S5.† Upon decomposing the SOC contribution into different excitations, it was found that the maximum SOC contribution to the D tensor mainly came from the excitations of the spin-pairing transitions (approximately 0.455 cm^{-1} at the ωB97X-D3 level, Table S5†), accompanied by an $\alpha \rightarrow \beta$ spin-flipping process, namely, quartet $\rightarrow$ doublet. This indicates a significant mixing of the excited D_1' state into the Q_1 state. Additionally, the D value was also expected to be negative (i.e., $D < 0$), implying a more "rod-like" spin density distribution that is "prolate" in shape, with the D_{zz} component of the ZFS tensor aligned parallel to the spin distribution within the carbazole plane,[54] see Fig. 7.

As a result, the ISC rate for TTM-1Cz-An was extremely fast due to the larger $f_s(m_2, m_4)$ value and the fact that the energy gaps between the D_1' and Q_1 states were sufficiently smaller than the vibrational quanta for any of the six allowed ($\Delta m_{2,4} = \pm 1$, ± 2) transitions (Fig. 6a). Consequently, the vibrational relaxation within the D_1' state was also very rapid, with the transition occurring between the zeroth vibrational levels of the D_1' and Q_1 states. In this case, the thermal energy of approximately 200 cm^{-1} at 298 K was most likely to significantly exceed $|3/2 J_{TR}|$, making the RISC from Q_1 to D_1' fully possible. This contrasts with scenarios involving a large energy gap, which are termed as the 'reversed-quartet mechanism'. Furthermore, the vibrational mixing between Q_1 and D_1' was investigated, with the
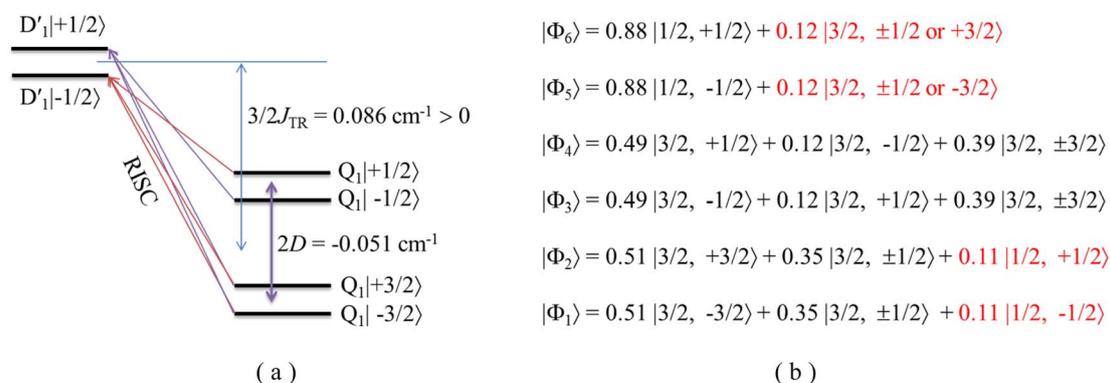
Fig. 6 (a) Visualization of the dynamic electron polarization generation via the D_1' and Q_1 quantum mixing states, which was constructed by a strong exchange coupling ($J > D$) between the doublet and triplet moieties; (b) projections of the eigenfunctions on the model space at the vibration coupling modes, here, $C^2|S, M_S\rangle$, where C^2 denotes the configuration weight coefficients, S is the spin quantum number, and M_S denotes the spin sublevels.

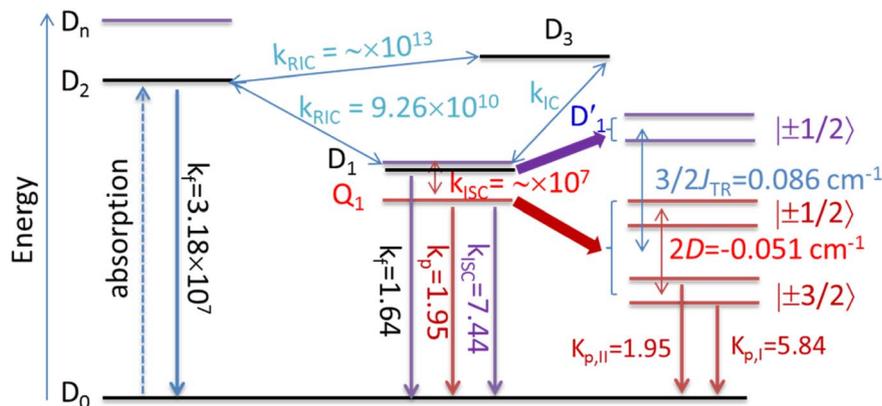**Fig. 8** Possible deactivation mechanisms of the excited states for the TTM-1Cz-An complex. Here, k_f denotes the fluorescence rate; k_p is phosphorescence rate; k_{ISC} represents the intersystem crossing rate; k_{IC} refers to the internal conversion rate; J_{TR} is the exchange coupling, and the zero-field splitting tensor is D. All the rate units are in s^{-1}.

projections of the eigenfunctions onto the model space at key vibrational coupling modes, as reported in Fig. 6b and Table S6.† It became evident that the Q_1 and states were no longer "pure" excited quartet and doublet states (represented by $|\Phi_n\rangle$),[53] but rather, the Q_1 substate was mixed with D'_1 by 11%, and similarly, the D'_1 states were mixed with Q_1 by 12%.

3.4.2 $D_1 \leftrightarrow Q_1$ RISC. The swift interconversion between the D'_1 and D_1 states was elucidated through EISC, ascribed to the inequality of the exchange interactions J_{13} and J_{12}, denoted as $\Delta J_{ST} = 0.174$ cm^{-1},[52] as detailed in Table 1. Nevertheless, the efficacious occurrence of RISC from Q_1 to D_1 states is pivotal in the luminescence control of the TTM-1Cz-An radical complex, with possible deactivation pathways of the excited states, as shown in Fig. 8. It is a well-established notion that the RISC rates k_{RISC} are predominantly dictated by three foundational factors: a strong SOC effect between the Q_1 and D_1 states, a diminutive energy gap $\Delta E(Q_1 - D_1)$, and a significant overlap of the vibrational wavefunctions between Q_1 and D_1. As anticipated, the computed adiabatic energy difference $\Delta E(Q_1 - D_1)$

for TTM-1Cz-An was notably small, approximately 745 cm^{-1} at the ωB97X-D3 level, which will be undoubtedly beneficial to augmenting the k_{RISC}. The SOC constants, which are highly dependent on the electronic configuration of the Q_1 and D_1 states, are summarized in Tables 2 and S7.† According to El-Sayed's rule,[55] the direct SOC interaction between Q_1 and D_1 is forbidden due to the violation of the total angular momentum conservation principle, resulting in an exceedingly minute SOC constant of $\langle Q_1|\hat{H}_{SOC}|D_1\rangle = 0.002$ cm^{-1} (see Table 2). Conversely, for those states with distinct transition characters, the SOC constants are comparatively larger, exemplified by $\langle Q_1|\hat{H}_{SOC}|D_0\rangle = 0.025$ cm^{-1}, and $\langle Q_1|\hat{H}_{SOC}|D_3\rangle = 0.093$ cm^{-1}. The inhibition SOC effect between Q_1 and D_1 would result in a relatively slow RISC rate of 2.41×10^1 s^{-1} at 298 K, as reported in Table 3. For meaningful RISC to occur, it is imperative that the k_{RISC} rate of 2.41×10^1 s^{-1} at room temperature has to be larger than the radiative ($kp = 1.95$ s^{-1}) and nonradiative ($k_{RISC} = 7.44$ s^{-1}, as listed in Fig. 8) rates of the Q_1 state to the ground D_0 state, which is patently insufficient.

Table 2 Spin−orbit coupling (SOC) matrix elements (cm^{-1}) between excited states of TTM-1Cz-An calculated at the CASSCF level. S is the spin quantum number; M_S denotes the spin sublevels

State 1	State 2	$\langle S_1 = 3/2, M_{s_1}|\hat{H}_{SOC}|S_2 = 1/2, M_{s_2}\rangle^a$	Total SOC^b
Q_1	D_0	$\langle S_1 = 3/2, 3/2|\hat{H}_{SOC}|S_2 = 1/2, 1/2\rangle = 0.013 + 0.006i$	0.025
		$\langle S_1 = 3/2, 1/2|\hat{H}_{SOC}|S_2 = 1/2, 1/2\rangle = -0.000 + 0.005i$	
		$\langle S_1 = 3/2, -1/2|\hat{H}_{SOC}|S_2 = 1/2, 1/2\rangle = 0.008 - 0.003i$	
Q_1	D_1	$\langle S_1 = 3/2, 3/2|\hat{H}_{SOC}|S_2 = 1/2, 1/2\rangle = -0.001 + 0.001i$	0.002
		$\langle S_1 = 3/2, 1/2|\hat{H}_{SOC}|S_2 = 1/2, 1/2\rangle = -0.000 - 0.000i$	
		$\langle S_1 = 3/2, -1/2|\hat{H}_{SOC}|S_2 = 1/2, 1/2\rangle = -0.000 - 0.000i$	
Q_1	D_2	$\langle S_1 = 3/2, 3/2|\hat{H}_{SOC}|S_2 = 1/2, 1/2\rangle = -0.003 + 0.003i$	0.008
		$\langle S_1 = 3/2, 1/2|\hat{H}_{SOC}|S_2 = 1/2, 1/2\rangle = -0.000 - 0.002i$	
		$\langle S_1 = 3/2, -1/2|\hat{H}_{SOC}|S_2 = 1/2, 1/2\rangle = -0.002 - 0.002i$	
Q_1	D_3	$\langle S_1 = 3/2, 3/2|\hat{H}_{SOC}|S_2 = 1/2, 1/2\rangle = 0.027 - 0.044i$	0.093
		$\langle S_1 = 3/2, 1/2|\hat{H}_{SOC}|S_2 = 1/2, 1/2\rangle = -0.000 + 0.028i$	
		$\langle S_1 = 3/2, -1/2|\hat{H}_{SOC}|S_2 = 1/2, 1/2\rangle = 0.015 + 0.026i$	

^{a} $\langle 3/2|\hat{H}_{SOC}|1/2\rangle = \langle -3/2|\hat{H}_{SOC}|-1/2\rangle$, $\langle 1/2|\hat{H}_{SOC}|1/2\rangle = \langle -1/2|\hat{H}_{SOC}|-1/2\rangle$, and $\langle -1/2|\hat{H}_{SOC}|1/2\rangle = \langle 1/2|\hat{H}_{SOC}|-1/2\rangle$. ^{b} SOC $= \left[\sum_{S, M_s} \langle \hat{H}_{SOC}\rangle^2\right]^{1/2}$.

Table 3 Obtained intersystem crossing (ISC, $D_1 \rightarrow Q_1$) and reverse intersystem crossing (RISC, $Q_1 \rightarrow D_1$) rates with and without the HT effect between the D_1 and Q_1 states from 80 to 298 K for TTM-1Cz-An; all units are in s^{-1}

Temp.	$k_{ISC}(D_1 \rightarrow Q_1)$				$k_{RISC}(Q_1 \rightarrow D_1)$			
	FC ($\times 10^2$)	FCHT ($\times 10^6$)			FC ($\times 10^1$)	FCHT ($\times 10^5$)		
	Average	$1/2 \rightarrow +3/2$	$1/2 \rightarrow +1/2$	$1/2 \rightarrow -1/2$	Average	$+3/2 \rightarrow 1/2$	$+1/2 \rightarrow 1/2$	$-1/2 \rightarrow 1/2$
298	5.85	7.89	2.28	2.45	2.41	6.64	2.07	2.22
150	6.65	8.98	2.59	2.78	4.58	8.76	2.53	2.72
80	6.78	9.16	2.65	2.84	7.31	9.12	2.64	2.83

To gain further insights, it becomes imperative to consider the vibronic SOC effects, often referred to as the Herzberg–Teller (HT) term. The first derivatives of the SOC constants with respect to the mass-weighted normal coordinates, $\partial \langle Q_1 | \hat{H}_{SOC} | D_1 \rangle / \partial Q_k$, at equilibrium geometry $Q_k = 0$ of the Q_1 state, were numerically computed using finite-difference methods, as illustrated in Fig. 9c, with the corresponding k_{RISC} rate constants enumerated in Table 3. It was observed that the RISC rate k_{RISC}, inclusive of the HT term, was 3.64×10^5 s^{-1} at 298 K, which was approximately four orders of magnitude greater than the FC rate of 2.41×10^1 s^{-1}, and significantly exceeded the

phosphorescence and nonradiative rates of the Q_1 state. This provides a condition for the repopulation of the D_1 state. With respect to the vibration modes, only a select few are instrumental in altering the vibrational structure and inducing a more pronounced SOC interaction. The representative modes of $\omega_{170} = 1423$ cm^{-1} and $\omega_{198} = 1684$ cm^{-1}, corresponding to the skeletal vibrations of the TTM-1Cz-An radical, were characterized by Huang–Rhys factors of $S_{170} = 0.019$ and $S_{198} = 0.008$, along with reorganization energies of $\lambda_{170} = 27.19$ cm^{-1} and $\lambda_{198} = 5.51$ cm^{-1}, respectively, as shown in Fig. 9 and Table S8.† These vibrations significantly enhance $\partial \langle Q_1 | \hat{H}_{SOC} | D_1 \rangle / \partial Q_k$
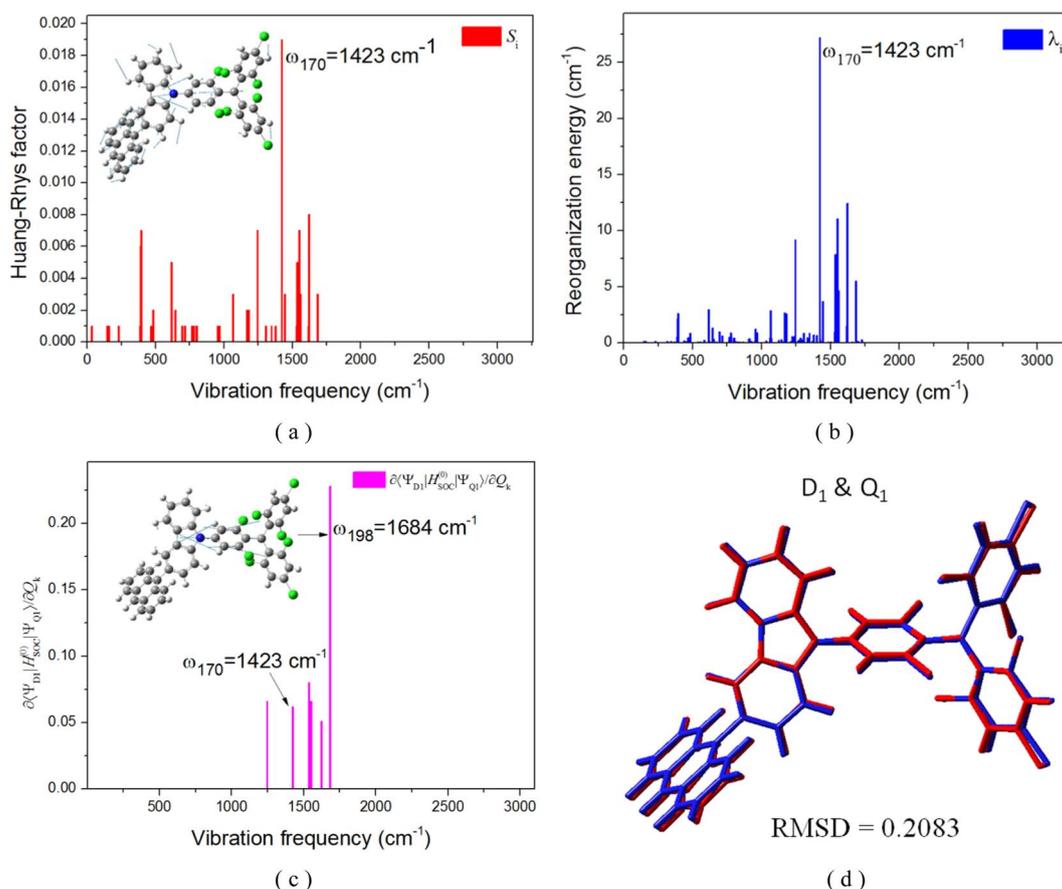

Fig. 9 Calculated Huang–Rhys factors (a) and reorganization energy (b) *versus* the normal vibration frequency between D_1 and Q_1 on the Q_1 potential energy surface, respectively; size of the SOC matrix element depends on the motion along the representative promotion vibration mode (c); (d) root-mean-squared deviations (RMSD) in Å between the D_1 and Q_1 geometries.
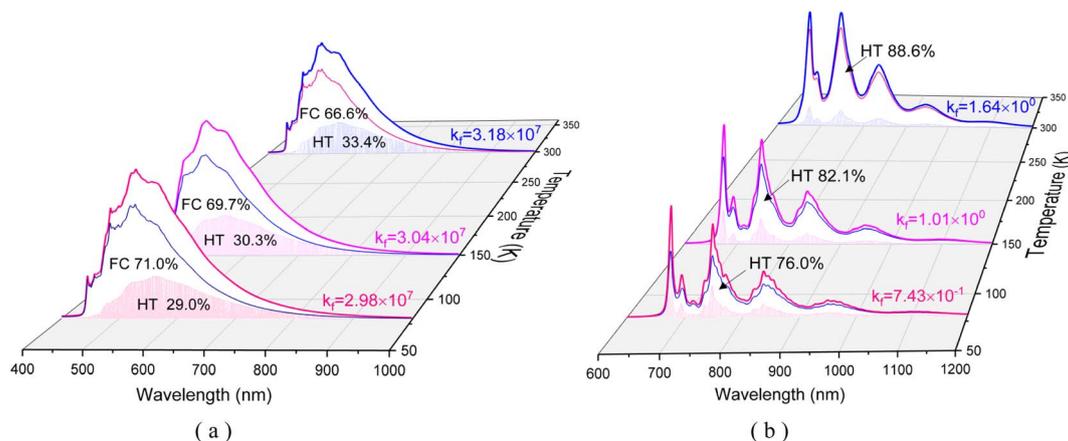
Fig. 10 Comparison diagrams of the contributions of the calculated HT and FC to the fluorescence spectra and radiation rates (k_f, unit in s^{-1}) for the excited D_2 state (a) and D_1 (b) states of TTM-1Cz-An at different temperatures.

due to the alterations in $\langle Q_1|\hat{H}_{SOC}|D_1 \rangle$ (for instance, 0.228 cm^{-1} for ω_{198}) as a result of the complete overlap of the molecular orbitals density pertinent to the $Q_1 \leftrightarrow D_1$ transition and the populations of the vibrational modes. Consequently, it is plausible to deduce that the vibronic SOC is the predominant coupling interaction facilitating RISC, and can remarkably enhance the RISC rates from Q_1 to D_1 by approximately four orders of magnitude.

3.5 Luminescence mechanism and internal conversion

In this section, we focus on the luminescence mechanism of the TTM-1Cz-An radical. The calculated fluorescence spectra and radiative rate constants (k_f, unit in s^{-1}) for the excited D_2 and D_1 states at different temperatures are presented Fig. 10 and S1.† It could be clearly seen that the D_1 state exhibited a weak visible emission at 670 nm, close to the experimental value of 685 nm, even when driven by the HT effect. This suggests a small oscillator strength for the $D_1 \rightarrow D_0$ emission, consistent with the inhibited $D_0 \rightarrow D_1$ absorption transition discussed in Section 3.1. These characteristics indicate a relatively slow radiative rate from the D_1 emission, $k_r = 1.64$ s^{-1} at 298 K, resulting in ineffective luminescence. To enhance the luminescence efficiency of the TTM-1Cz-An radical compound, the D_1 state must undergo reverse internal conversion and be effectively distributed to the D_2 and D_3 states, which possess a high oscillator strength, or alternatively, "borrow intensity"

from the luminescent D_2 state.[10,11] Based on the perturbation theory of intensity borrowing, the small energy gaps between excited states (as seen Table S9†) involved in the internal conversion mechanism are likely to result in a significant mixing between states with doublet multiplicity, as indicated by the calculated electronic coupling interactions ($V_{D_{n,m}}$) using the two-state generalized Mulliken–Hush approximation, and the $V_{D_{n,m}}$ values are listed in Table 4.[45] The corresponding internal conversion rate constants, $k_{(R)IC}$ were also estimated and are listed in Table 5.

The electronic coupling $V_{D_{1,2}}$ of the D_1 and D_2 states was notably strong, with an interaction of 37.4 meV at the ωB97X-D3 level, see Table 4. This leads to larger internal conversion rates $k_{(R)IC}$ from $D_1 \leftrightarrow D_2$. It could be observed from Table 5 that the $k_{RIC}(D_1 \rightarrow D_2)$ rate was approximately 9.26×10^{10} s^{-1} at 298 K, which was roughly four orders of magnitude larger than the ISC rate from D_1 to Q_1, 7.89×10^6 s^{-1}. This indicates that the D_2 state is effectively populated at room temperature. Furthermore, it could be noted that the large $k_{RIC}(D_1 \rightarrow D_2)$ rate of 9.26×10^{10} s^{-1} was predominantly influenced by a single vibrational mode "ω_{197}" at 1673 cm^{-1}, corresponding to the in-plane stretching vibration of the carbazole skeleton, as depicted in Fig. S2.† This frequency also matched the energy gap $\Delta E(D_1 \rightarrow D_2)$ (Table S9†), which is crucial for significantly enhancing the RIC rate. Interestingly, the D_2 and D_3 states were closely matched in energy and both originated from local excitation on

Table 4 Parameters of the calculated electronic coupling interactions ($V_{D_{n,m}}$) between the excited states using the two-state generalized Mulliken–Hush approximation

Method	Transition state	$\mu(D_{n,m})$/a.u.	$\Delta\mu(D_{n,m})$/a.u.	$\Delta E(D_{n,m})$/eV	$V_{D_{n,m}}$/meV
ωb97X-D3	$D_1 \rightarrow D_2$	0.09899	2.29722	0.871	$\langle D_1|\hat{H}_V|D_2 \rangle = 37.39$
	$D_1 \rightarrow D_3$	0.00134	0.64148	0.951	$\langle D_1|\hat{H}_V|D_3 \rangle = 1.99$
	$D_2 \rightarrow D_3$	0.68266	1.65574	0.080	$\langle D_2|\hat{H}_V|D_3 \rangle = 24.33$
CAM-B3LYP	$D_1 \rightarrow D_2$	0.12389	4.65726	0.735	$\langle D_1|\hat{H}_V|D_2 \rangle = 19.52$
	$D_1 \rightarrow D_3$	0.00247	0.54122	0.953	$\langle D_1|\hat{H}_V|D_3 \rangle = 4.35$
	$D_2 \rightarrow D_3$	0.61762	4.11604	0.218	$\langle D_2|\hat{H}_V|D_3 \rangle = 31.33$

Table 5 Calculated internal conversion nonradiative rates (k_{IC}, unit in s^{-1}) between the D$_1$ and D$_2$ (or D$_3$) states from 80 to 298 K for TTM-1Cz-An

Temp.	$k_{RIC}(D_1 \rightarrow D_2)$	$k_{IC}(D_2 \rightarrow D_1)$	$k_{RIC}(D_2 \rightarrow D_3)$	$k_{IC}(D_3 \rightarrow D_2)$	$k_{IC}(D_3 \rightarrow D_1)^a$
ωB97X-D3/def2-TZVP					
298	9.26×10^{10}	1.95×10^{12}	1.13×10^{13}	6.12×10^{13}	3.45×10^{10}
150	6.55×10^{9}	1.67×10^{12}	3.38×10^{13}	8.79×10^{13}	3.46×10^{10}
80	1.30×10^{9}	1.59×10^{12}	6.93×10^{13}	1.14×10^{14}	3.49×10^{10}
CAM-B3LYP/def2-TZVP					
298	5.90×10^{10}	5.35×10^{11}	8.43×10^{13}	9.48×10^{13}	8.28×10^{10}
150	3.04×10^{10}	4.58×10^{11}	6.20×10^{13}	2.43×10^{14}	7.78×10^{10}
80	2.28×10^{10}	4.39×10^{11}	4.65×10^{13}	3.43×10^{14}	7.50×10^{10}

^{a} $k_{RIC}(D_1 \rightarrow D_3)$ was estimated but obtained an unreasonable value due to the significant activation energy gap and so is not listed.

the TTM-1Cz moiety, as shown in Fig. 2, allowing for rapid interconversion into resonant states. Regarding the fluorescence emission of the D$_2$ state, as illustrated in Fig. 10, TTM-1Cz-An was capable of generating effective radiative fluorescence. Here, the calculated emission rate $k_f = 2.98$ to 3.18×10^7 s^{-1} was in good agreement with the experimental value of 1.28×10^7 s^{-1},[56] and its temperature dependence was negligible. The aforementioned discussions provide the possible mechanisms for the optical readout of the stable TTM-1Cz-An radical in applications such as OLEDs and quantum-information technologies.

4. Conclusions

A thorough understanding of the molecular factors that control the fluorescence emission of organic radicals is essential for the design of a new generation of efficient radical emitters. To this end and to gain a comprehensive and systematic understanding of the luminescence mechanism of the TTM-1Cz-An radical, we employed quantum theoretical calculations to quantitatively predict the photophysical properties of TTM-1Cz-An radical, including the fluorescence emission rates, optical spectrum, and excited-state dynamics.

Our calculated results showed that the photoexcited sing-doublet D$_1$ state from the anthracene singlet excited state was quickly converted to the doublet D$_1'$ state by EISC with the help of the exchange-induced spin conversion, facilitated by the significant exchange interactions of $J_{13} = 0.232$ and $J_{12} = -0.116$ cm^{-1}. In this process, the total spin multiplicity is conserved during the D$_1 \rightarrow$ D$_1'$ transition. Subsequently, the D$_1'$ state can evolve into a quartet state by the exchange coupling $3/2 J_{TR} = 0.086$ cm^{-1} between the triplet spin electrons of anthracene and the TTM-1Cz radical, which exceeds the zero-field splitting tensor of $D = 0.026$ cm^{-1}. The direct SOC-induced ISC to the Q$_1$ state was minimal due to the nearly identical spatial wavefunctions of the D$_1'$ and Q$_1$ levels. It is well known that the effective occurrence of RISC from Q$_1$ to D$_1$ states is a critical rate-determining step in controlling the luminescence of the TTM-1Cz-An radical complex. The calculated RISC rate, including the HT effect, was $k_{RISC} = 3.64 \times 10^5$ s^{-1} at 298 K, which was approximately four orders of magnitude greater than the FC rate of 2.41×10^1 s^{-1}, and far greater than the phosphorescence and nonradiative rates of the Q$_1$ state, thus enabling the repopulation of the D$_1$ state. However, the D$_1$ emission exhibited a relatively slow radiative rate of $k_r = 1.64$ s^{-1} at 298 K, resulting in ineffective luminescence. For the TTM-1Cz-An radical to exhibit effective luminescence, the D$_1$ state must undergo reverse internal conversion and be effectively populated into the D$_2$ or D$_3$ states. In the case of the D$_2$ state redistribution, there was a strong electronic coupling of 37.4 meV between the D$_1$ and D$_2$ states with a dense manifold of doublet states energetically close to the D$_1$ state, leading to a larger reverse internal conversion rate of $k_{RIC} = 9.26 \times 10^{10}$ s^{-1} into the D$_2$ state. The calculated D$_2$ emission rate of $k_f = 2.98$ to 3.18×10^7 s^{-1} was in good agreement with the experimental value of 1.28×10^7 s^{-1}. Our study provides valuable information on the radical luminescence mechanism, which will be helpful for the development of novel radical luminescent materials.

Data availability

The data supporting the findings of this study are available within the article and in the ESI.†

Conflicts of interest

All authors declare that they have no conflicts of interest.

Acknowledgements

References

1 Z. Y. Yang, Z. Mao, Z. L. Xie, Y. Zhang, S. W. Liu, J. Zhao, J. R. Xu, Z. G. Chi and M. P. Aldred, Recent advances in organic thermally activated delayed fluorescence materials, *Chem. Soc. Rev.*, 2017, **46**, 915–1016.

2 J. H. Kim, J. H. Yun and J. Y. Lee, Recent Progress of Highly Efficient Red and Near-Infrared Thermally Activated Delayed Fluorescent Emitters, *Adv. Opt. Mater.*, 2018, **6**, 1800255.

3 J. M. Teng, Y. F. Wang and C. F. Chen, Recent progress of narrowband TADF emitters and their applications in OLEDs, *J. Mater. Chem. C*, 2020, **8**, 11340–11353.

4 Y. Xu, P. Xu, D. Hu and Y. Ma, Recent progress in hot exciton materials for organic light-emitting diodes, *Chem. Soc. Rev.*, 2021, **50**, 1030–1069.

5 H. Guo, Q. Peng, X. K. Chen, Q. Gu, S. Dong, E. W. Evans, A. J. Gillett, X. Ai, M. Zhang, D. Credgington, V. Coropceanu, R. H. Friend, J.-L. Brédas and F. Li, High Stability and Luminescence Efficiency in Donor–Acceptor Neutral Radicals not Following the Aufbau Principle, *Nat. Mater.*, 2019, **18**, 977–984.

6 H. Uoyama, K. Goushi, K. Shizu, H. Nomura and C. Adachi, Highly efficient organic light-emitting diodes from delayed fluorescence, *Nature*, 2012, **492**, 234–238.

7 Y. Tao, K. Yuan, T. Chen, P. Xu, H. H. Li, R. F. Chen, C. Zheng, L. Zhang and W. Huang, Thermally Activated Delayed Fluorescence Materials Towards the Breakthrough of Organo electronics, *Adv. Mater.*, 2014, **26**, 7931–7958.

8 R. Czerwieniec, M. J. Leitl, H. H. H. Homeier and H. Yersin, Cu(I) complexex-Thermally activated delayed fluorescence. Photophysical approach and material design, *Coord. Chem. Rev.*, 2016, **325**, 2–28.

9 L. Ji, J. Q. Shi, J. Wei, T. Yu and W. Huang, Air-Stable Organic Radicals: New-Generation Materials for Flexible Electronics?, *Adv. Mater.*, 2020, **32**, 1908015.

10 E. Cho, V. Coropceanu and J.-L. Brédas, Organic Neutral Radical Emitters: Impact of Chemical Substitution and Electronic-State Hybridization on the Luminescence Properties, *J. Am. Chem. Soc.*, 2020, **142**, 17782–17786.

11 A. Abdurahman, T. J. H. Hele, Q. Gu, J. Zhang, Q. Peng, M. Zhang, R. H. Friend, F. Li and E. W. Evans, Understanding the Luminescent Nature of Organic Radicals for Efficient Doublet Emitters and Pure-Red Light-Emitting Diodes, *Nat. Mater.*, 2020, **19**, 1224–1229.

12 H. Abroshan, V. Coropceanu and J.-L. Brédas, Radiative and Nonradiative Recombinations in Organic Radical Emitters: The Effect of Guest–Host Interactions, *Adv. Funct. Mater.*, 2020, **30**, 2002916.

13 V. Gamero, D. Velasco, S. Latorre, F. López-Calahorra, E. Brillas and L. Juliá, [4-(N-Carbazolyl)-2,6-dichlorophenyl]bis(2,4,6-tri-chlorophenyl)methyl Radical an Efficient Red Light-Emitting Paramagnetic Molecule, *Tetrahedron Lett.*, 2006, **47**, 2305–2309.

14 Q. Peng, A. Obolda and M. Z. F. Li, Organic Light-Emitting Diodes Using a Neutral π Radical as Emitter: The Emission from a Doublet, *Angew. Chem., Int. Ed.*, 2015, **54**, 7091–7095.

15 X. Ai, E. W. Evans, S. Dong, A. J. Gillett, H. Guo, Y. Chen, T. J. H. Hele, R. H. Friend and F. Li, Efficient Radical-based Light-Emitting Diodes with Doublet Emission, *Nature*, 2018, **563**, 536–540.

16 E. Cho and V. Coropceanu, Jean-Luc Brédas, Impact of chemical modifications on the luminescence properties of

organic neutral radical emitters, *J. Mater. Chem. C*, 2021, **9**, 10794–10801.

17 S. Gorgon, K. Lv, J. Grüne, B. H. Drummond, W. K. Myers, G. Londi, G. Ricci, D. Valverde, C. Tonnelé, P. Murto, A. S. Romanov, D. Casanova, V. Dyakonov, A. Sperlich, D. Beljonne, Y. Olivier, L. Feng, R. H. Friend and E. W. Evans, Reversible spin-optical interface in luminescent organic radicals, *Nature*, 2023, **62**, 538–544.

18 Y. Teki, Excited-state dynamics of non-luminescent and luminescent π-radicals, *Chemistry*, 2020, **26**, 980–996.

19 M. Atzori and R. Sessoli, The second quantum revolution: role and challenges of molecular chemistry, *J. Am. Chem. Soc.*, 2019, **141**, 11339–11352.

20 A. Gaita-Ariño, F. Luis, S. Hill and E. Coronado, Molecular spins for quantum computation, *Nat. Chem.*, 2019, **11**, 301–309.

21 T. Quintes, M. Mayländer and S. Richert, Properties and applications of photoexcited chromophore–radical systems, *Nat. Rev. Chem.*, 2023, **7**, 75–90.

22 F. Neese, Software update: the ORCA 5.0 program system, version 4.0, *Wiley Interdiscip. Rev.: Comput. Mol. Sci.*, 2018, **8**, e1327.

23 Y.-S. Lin, G.-D. Li, S.-P. Mao and J.-D. Chai, Long-Range Corrected Hybrid Density Functionals with Improved Dispersion Corrections, *J. Chem. Theory Comput.*, 2013, **9**, 263–272.

24 T. Yanai, D. P. Tew and N. C. Handy, A new hybrid exchange-correlation functional using the Coulomb-attenuating method (CAM-B3LYP), *Chem. Phys. Lett.*, 2004, **393**, 51–57.

25 A. D. Becke, Density-functional exchange-energy approximation with correct asymptotic behavior, *Phys. Rev. A*, 1988, **38**, 3098–3100.

26 O. Vahtras, J. Almlöf and M. W. Feyereisen, Integral approximations for LCAO-SCF calculations, *Chem. Phys. Lett.*, 1993, **213**, 514–518.

27 F. Weigend and R. Ahlrichs, Balanced basis sets of split valence triple zeta valence and quadruple zeta valence quality for H to Rn: Design and assessment of accuracy, *Phys. Chem. Chem. Phys.*, 2005, **7**, 3297–3305.

28 F. Neese, F. Wennmohs, A. Hansen and U. Becker, Efficient, approximate and parallel Hartree−Fock and hybrid DFT calculations. A 'chain-of-spheres' algorithm for the Hartree−Fock exchange, *Chem. Phys.*, 2009, **356**, 98–109.

29 D. M. York and M. Karplus, A Smooth Solvation Potential Based on the Conductor-Like Screening Model, *J. Phys. Chem. A*, 1999, **103**, 11060–11079.

30 T. Schwabe and L. Goerigk, Time-dependent double-hybrid density functionals with spin-component and spin-opposite scaling, *J. Chem. Theory Comput.*, 2017, **13**, 4307–4323.

31 M. Casanova-Páez, M. B. Dardis and L. Goerigk, ωB2PLYP and ωB2GPPLYP: The first two double-hybrid density functionals with long-range correction optimized for excitation energies, *J. Chem. Theory Comput.*, 2019, **15**, 4735–4744.

32 M. Casanova-Páez and L. Goerigk, Time-dependent long-range-corrected double-hybrid density functionals with

spin-component and spin-opposite scaling: a comprehensive analysis of singlet-singlet and singlet-triplet excitation energies, *J. Chem. Theory Comput.*, 2021, **17**, 5165–5186.

33 Y. Guo, C. Riplinger, U. Becker, D. G. Liakos, Y. Minenkov, L. Cavallo and F. Neese, Communication: An improved linear scaling perturbative triples correction for the domain based local pair-natural orbital based singles and doubles coupled cluster method [DLPNO-CCSD(T)], *J. Chem. Phys.*, 2018, **148**, 011101.

34 Y. Guo, C. Riplinger, D. G. Liakos, U. Becker, M. Saitow and F. Neese, Linear scaling perturbative triples correction approximations for open-shell domain-based local pair natural orbital coupled cluster singles and doubles theory [DLPNO-CCSD(T0/T)], *J. Chem. Phys.*, 2020, **152**, 024116.

35 C. Angeli, S. Borini, M. Cestari and R. Cimiraglia, A quasidegenerate formulation of the second order n-electron valence state perturbation theory approach, *J. Chem. Phys.*, 2004, **121**, 4043–4049.

36 S. F. Boys, Construction of some molecular orbitals to be approximately invariant for changes from one molecule to another, *Rev. Mod. Phys.*, 1960, **32**, 296.

37 M. Franz, F. Neese and S. Richert, Calculation of exchange couplings in the electronically excited state of molecular three-spin systems, *Chem. Sci.*, 2022, **13**, 12358–12366.

38 D. Reta, I. P. R. de Moreira and F. Illas, Magnetic Coupling Constants in Three Electrons Three Centers Problems from Effective Hamiltonian Theory and Validation of Broken Symmetry-Based Approaches, *J. Chem. Theory Comput.*, 2016, **12**, 3228–3235.

39 F. Neese, Importance of Direct Spin−Spin Coupling and Spin-Flip Excitations for the Zero-Field Splittings of Transition Metal Complexes: A Case Study, *J. Am. Chem. Soc.*, 2006, **128**, 10213–10222.

40 B. Minaev, G. Baryshnikov and H. Ågren, Principles of phosphorescent organic light emitting devices, *Phys. Chem. Chem. Phys.*, 2014, **16**, 1719–1758.

41 M. Roemelt, D. Maganas, S. DeBeer and F. Neese, A combined DFT and restricted open-shell configuration interaction method including spin-orbit coupling: Application to transition metal L-edge X-ray absorption spectroscopy, *J. Chem. Phys.*, 2013, **138**, 204101.

42 F. Neese, Efficient and accurate approximations to the molecular spin-orbit coupling operator and their use in molecular g-tensor calculations, *J. Chem. Phys.*, 2005, **122**, 034107.

43 M. C. Daza, M. Doerr, S. Salzmann, C. M. Marian and W. Thiel, Photophysics of phenalenone: quantum mechanical investigation of singlet–triplet intersystem crossing, *Phys. Chem. Chem. Phys.*, 2009, **11**, 1688–1696.

44 V. Coropceanu, X. K. Chen, T. Wang, Z. Zheng and J. L. Brédas, Charge-Transfer Electronic States in Organic Solar Cells, *Nat. Rev. Mater.*, 2019, **4**, 689–707.

45 R. J. Cave and M. D. Newton, Generalization of the Mulliken-Hush Treatment for the Calculation of Electron Transfer Matrix Elements, *Chem. Phys. Lett.*, 1996, **249**, 15–19.

46 Y. L. Niu, Q. Peng, C. Deng, X. Gao and Z. G. Shuai, Theory of Excited State Decays and Optical Spectra: Application to Polyatomic Molecules, *J. Phys. Chem. A*, 2010, **114**, 7817–7831.

47 L. L. Lv, K. Yuan, T. Y. Zhao and Y. C. Wang, A new mechanistic study of a second generation TADF material based on the path integral approach incorporating Herzberg–Teller and Duschinsky rotation effects, *J. Mater. Chem. C*, 2020, **8**, 10369–10381.

48 B. de Souza, F. Neese and R. Izsák, On the theoretical prediction of fluorescence rates from first principles using the path integral approach, *J. Chem. Phys.*, 2018, **148**, 034104.

49 B. de Souza, G. Farias, F. Neese and R. Izsák, Predicting Phosphorescence Rates of Light Organic Molecules Using Time-Dependent Density Functional Theory and the Path Integral Approach to Dynamics, *J. Chem. Theory Comput.*, 2019, **15**, 1896–1904.

50 A. Baiardi, J. Bloino and V. Barone, General Time Dependent Approach to Vibronic Spectroscopy Including Franck–Condon, Herzberg–Teller, and Duschinsky Effects, *J. Chem. Theory Comput.*, 2013, **9**, 4097–4115.

51 M. Mayländer, T. Quintes, M. Franz, X. Allonas, A. V. Jentzsch and S. Richert, Distance dependence of enhanced intersystem crossing in BODIPY–nitroxide dyads, *Chem. Sci.*, 2023, **14**, 5361–5536.

52 Y. E. Kandrashkin and A. van der Est, Enhanced Intersystem Crossing due to Resonant Energy Transfer to a Remote Spin, *J. Phys. Chem. Lett.*, 2021, **12**, 7312–7318.

53 V. Rozenshtein, A. Berg, E. Stavitski, H. Levanon, L. Franco and C. Corvaja, Electron Spin Polarization of Functionalized Fullerenes. Reversed Quartet Mechanism, *J. Phys. Chem. A*, 2005, **109**(49), 11144–11154.

54 S. Richert, C. E. Tait and C. R. Timmel, Delocalisation of photoexcited triplet states probed by transient EPR and hyperfine spectroscopy, *J. Magn. Reson.*, 2017, **280**, 103–116.

55 M. A. El-Sayed, Spin-orbit coupling and the radiationless processes in nitrogen heterocyclics, *J. Chem. Phys.*, 1963, **38**, 2834–2838.

56 A. Abdurahman, T. J. H. Hele, Q. Gu, J. Zhang, Q. Peng, M. Zhang, R. H. Friend, F. Li and E. W. Evans, Understanding the Luminescent Nature of Organic Radicals for Efficient Doublet Emitters and Pure-Red Light-Emitting Diodes, *Nat. Mater.*, 2020, **19**, 1224–1229.